AFRL-OSR-VA-TR-2015-0120

DEVELOPMENT OF NEW PHOTOREFRACTIVE POLYMER MATERIALS

Nasser Peyghambarian
ARIZONA UNIV BOARD OF REGENTS TUCSON

05/19/2015
Final Report

Air Force Research Laboratory
AF Office Of Scientific Research (AFOSR)/ RTD
Arlington, Virginia 22203
Air Force Materiel Command

REPORT DOCUMENTATION PAGE

Form Approved
OMB No. 0704-0188

PLEASE DO NOT RETURN YOUR FORM TO THE ABOVE ORGANIZATION.

1. REPORT DATE *(DD-MM-YYYY)*	2. REPORT TYPE	3. DATES COVERED *(From - To)*
08-05-2015	Final Performance Report	01-05-2010 - 30-04-2015

4. TITLE AND SUBTITLE
Development of New Photorefractive Polymer Materials

5a. CONTRACT NUMBER
FA9550-10-1-0207

5b. GRANT NUMBER
FA9550-10-1-0207

5c. PROGRAM ELEMENT NUMBER

6. AUTHOR(S)
Blanche, P.-A., Norwood, R. A., and Peyghambarian, N.

5d. PROJECT NUMBER

5e. TASK NUMBER

5f. WORK UNIT NUMBER

7. PERFORMING ORGANIZATION NAME(S) AND ADDRESS(ES)
University of Arizona
888 N. Euclid Ave.
Tucson, AZ 85719-4824

8. PERFORMING ORGANIZATION REPORT NUMBER

9. SPONSORING/MONITORING AGENCY NAME(S) AND ADDRESS(ES)
Air Force Office of Scientific Research
875 N. Randolph St., Room 3112
Arlington, VA 22203

10. SPONSOR/MONITOR'S ACRONYM(S)
AFOSR

11. SPONSOR/MONITOR'S REPORT NUMBER(S)

12. DISTRIBUTION/AVAILABILITY STATEMENT
Approved for Public Release

13. SUPPLEMENTARY NOTES

14. ABSTRACT
The goal of this program was to develop highly efficient photorefractive (PR) polymer material for applications of interest to the Air Force. During the period of this report, we have demonstrated a new interdigitated coplanar geometry for the electrodes of the photorefractive device that enhances its sensitivity and allows diffraction with symmetrically incident beams, a configuration that was not possible with the conventional top and bottom electrodes. Related to this new electrode configuration, we measured the electric field strength inside the material with the help of a multiphoton microscope and were able to identify unsuspected asymmetry due to the photoconduction properties of the polymer matrix. The observed field nonlinearity has led to a revision of the theory governing the diffraction efficiency with coplanar electrode.

15. SUBJECT TERMS
photorefractive polymers, holographic display, 3D, coplanar interdigitated electrodes

16. SECURITY CLASSIFICATION OF:			17. LIMITATION OF ABSTRACT	18. NUMBER OF PAGES	19a. NAME OF RESPONSIBLE PERSON
a. REPORT	b. ABSTRACT	c. THIS PAGE			Nasser Peyghambarian
Unclassified	Unclassified	Unclassified	Unlimited	34	19b. TELEPHONE NUMBER *(Include area code)* 520-621-4649

Reset

INSTRUCTIONS FOR COMPLETING SF 298

1. REPORT DATE. Full publication date, including day, month, if available. Must cite at least the year and be Year 2000 compliant, e.g. 30-06-1998; xx-06-1998; xx-xx-1998.

2. REPORT TYPE. State the type of report, such as final, technical, interim, memorandum, master's thesis, progress, quarterly, research, special, group study, etc.

3. DATES COVERED. Indicate the time during which the work was performed and the report was written, e.g., Jun 1997 - Jun 1998; 1-10 Jun 1996; May - Nov 1998; Nov 1998.

4. TITLE. Enter title and subtitle with volume number and part number, if applicable. On classified documents, enter the title classification in parentheses.

5a. CONTRACT NUMBER. Enter all contract numbers as they appear in the report, e.g. F33615-86-C-5169.

5b. GRANT NUMBER. Enter all grant numbers as they appear in the report, e.g. AFOSR-82-1234.

5c. PROGRAM ELEMENT NUMBER. Enter all program element numbers as they appear in the report, e.g. 61101A.

5d. PROJECT NUMBER. Enter all project numbers as they appear in the report, e.g. 1F665702D1257; ILIR.

5e. TASK NUMBER. Enter all task numbers as they appear in the report, e.g. 05; RF0330201; T4112.

5f. WORK UNIT NUMBER. Enter all work unit numbers as they appear in the report, e.g. 001; AFAPL30480105.

6. AUTHOR(S). Enter name(s) of person(s) responsible for writing the report, performing the research, or credited with the content of the report. The form of entry is the last name, first name, middle initial, and additional qualifiers separated by commas, e.g. Smith, Richard, J, Jr.

7. PERFORMING ORGANIZATION NAME(S) AND ADDRESS(ES). Self-explanatory.

8. PERFORMING ORGANIZATION REPORT NUMBER. Enter all unique alphanumeric report numbers assigned by the performing organization, e.g. BRL-1234; AFWL-TR-85-4017-Vol-21-PT-2.

9. SPONSORING/MONITORING AGENCY NAME(S) AND ADDRESS(ES). Enter the name and address of the organization(s) financially responsible for and monitoring the work.

10. SPONSOR/MONITOR'S ACRONYM(S). Enter, if available, e.g. BRL, ARDEC, NADC.

11. SPONSOR/MONITOR'S REPORT NUMBER(S). Enter report number as assigned by the sponsoring/ monitoring agency, if available, e.g. BRL-TR-829; -215.

12. DISTRIBUTION/AVAILABILITY STATEMENT. Use agency-mandated availability statements to indicate the public availability or distribution limitations of the report. If additional limitations/ restrictions or special markings are indicated, follow agency authorization procedures, e.g. RD/FRD, PROPIN, ITAR, etc. Include copyright information.

13. SUPPLEMENTARY NOTES. Enter information not included elsewhere such as: prepared in cooperation with; translation of; report supersedes; old edition number, etc.

14. ABSTRACT. A brief (approximately 200 words) factual summary of the most significant information.

15. SUBJECT TERMS. Key words or phrases identifying major concepts in the report.

16. SECURITY CLASSIFICATION. Enter security classification in accordance with security classification regulations, e.g. U, C, S, etc. If this form contains classified information, stamp classification level on the top and bottom of this page.

17. LIMITATION OF ABSTRACT. This block must be completed to assign a distribution limitation to the abstract. Enter UU (Unclassified Unlimited) or SAR (Same as Report). An entry in this block is necessary if the abstract is to be limited.

Development of New Photorefractive Polymer Materials
Grant FA9550-10-1-0207
Final report

Author: P.-A. Blanche

PIs: R. A. Norwood and N. Peyghambarian

Abstract

The goal of this program was to develop highly efficient photorefractive (PR) polymer material for applications of interest to the Air Force.

During the period of this report, we have demonstrated a new interdigitated coplanar geometry for the electrodes of the photorefractive device that enhances its sensitivity and allows diffraction with symmetrically incident beams, a configuration that was not possible with the conventional top and bottom electrodes (Section 1).

Related to this new electrode configuration, we measured the electric field strength inside the material with the help of a multiphoton microscope and were able to identify unsuspected asymmetry due to the photoconduction properties of the polymer matrix. The observed field nonlinearity has lead to a revision of the theory governing the diffraction efficiency with coplanar electrode (Section 2).

Section 3 describes the work done in collaboration with Dr. Evan's team at AFRL on the topic of competing gratings due to different charge species mobility. It was found that the application of a high electric field can be beneficial to the beam coupling, due to the higher mobility of the electron species that no longer contribute to the competitive grating at higher applied electric field.

Recent material advancements include the investigation of new sensitizers such as functionalized reduced graphene oxide, perylene diimides and iron complex. Measurements and findings in that regard are presented in Section 4.

Section 5 describes the direct fringe writing experiment that has been done by Prof. Bove's group at MIT using photorefractive material developed during this program. An optical architecture for updatable photorefractive polymer-based holographic displays via the direct fringe writing of computer-generated holograms has been demonstrated.

The last topic reported in Section 6 is the measurement of the PR material response according the the pulse temporal width over 9 orders of magnitude. We measured the diffraction efficiency by recording the diffraction of single pulses with durations from nanoseconds to seconds. Results indicate two modes of operation in PR materials: for long pulses with low peak power, the charges can be excited multiple times during the length of the pulse, while for a very short pulse with high peak power, the charges are only excited once before they are trapped. This single excitation generates a lower duty cycle grating and reduces the efficiency.

Introduction

Photorefractive materials change their index of refraction upon illumination through a series of electronic phenomena that make these materials one of the most intriguing and complex organic optical system. The optical response involves charge generation, photocondution, trapping, molecular alignment and nonlinear optics (Figure 1).

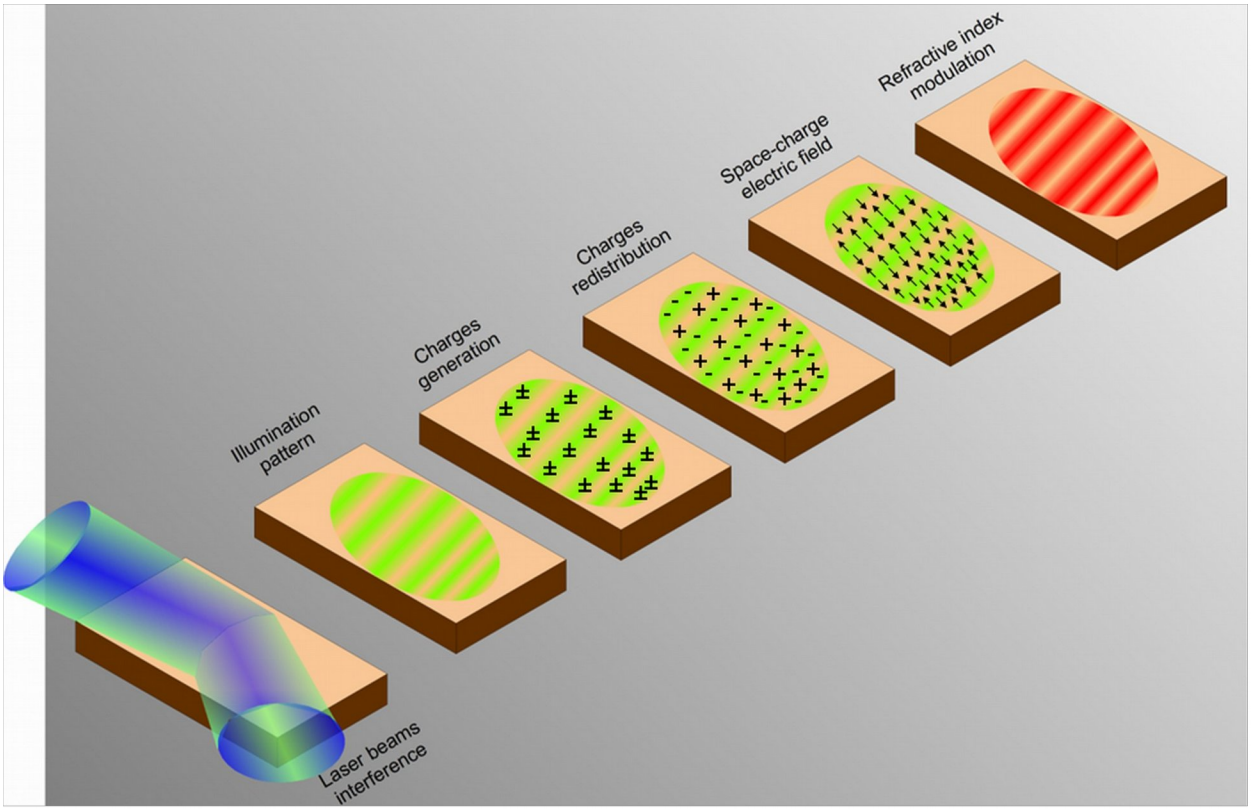

Figure 1: Basic steps of index modulation formation in photorefractive materials.

The refractive index change in photorefractive materials is dynamic and fully reversible, making these materials very interesting for a large variety of applications. Moreover the phase shift between the illumination pattern and the index modulation allows for dynamic beam coupling and amplification, unique characteristics that leads to novel capabilities.

The polymeric nature of the material we are studying allows large sample to be made. Lately, we demonstrated a holographic 3D display based on photorefractive polymers with a screen size up to 12x12 inch^2, a dimension that it is not possible to achieve with crystalline material.

In the present study we have developed original approaches and new material to improve the figures of merit of photorefractive polymers.

1. Coplanar electrodes:

Since the discovery of photorefractive polymer in 1991, the external electric field has always been applied with electrodes located at the top and bottom of the polymer film as illustrated in Figure 2a. This configuration prevents the use of symmetrically incident beams for writing a grating, because the field is orthogonal to the grating vector. If we try to do so, the charges generated in the bright regions are driven by the applied field directly to the electrodes and have no chance to stop in the dark regions to establish the space-charge field.

Because of this property, all the measurements and all the applications using photorefractive polymers are performed with a tilted sample geometry. In that configuration the recording beams have different angles of incident (figure 2b). The larger the blaze angle, the larger the diffraction efficiency.

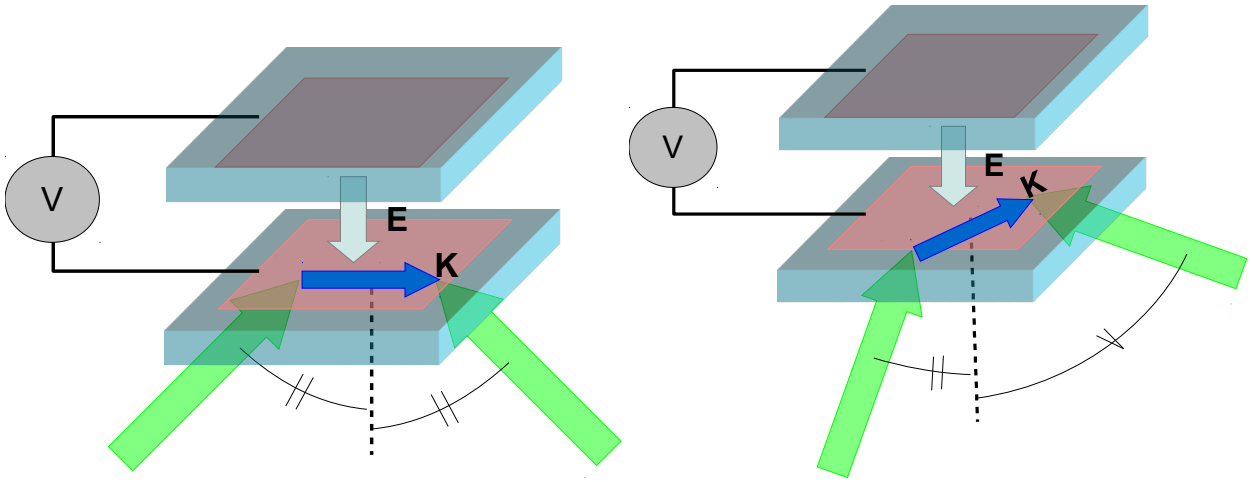

Figure 2: Regular electrode geometry with top and bottom ITO coated glass. a. symmetrical recording .b. tilted recording.

We introduced a paradigm shift by changing the geometry of the electrodes to a coplanar interdigitated geometry. In this configuration, both the positive and ground electrodes are located on the same glass plate, and have the shape of two combs interpenetrating each other (see Figure 3).

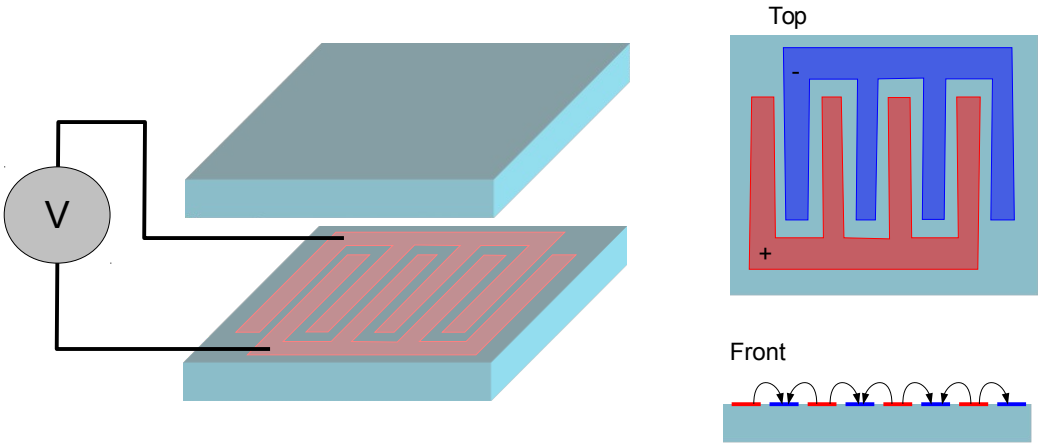

Figure 3: Interdigitated electrodes geometry. Isometric view, top view, and front view.

A major difference with the coplanar geometry is that now the external electric field arcs from one electrode to its neighbors outside the plane of the electrodes. Since the field is no longer parallel to the grating vector, it is possible to write holographic gratings with symmetrically incident beams, which was previously impossible.

We demonstrate this concept using the polymer host matrix poly (acrylic tetraphenyldiaminobiphenyl, PATPD). The chromophore 3-(N,N-di-n-butylaniline-4-yl)-1-dicyanomethylidene-2-cyclohexene (DBDC) provides the refractive index change, and C60 and N-ethylcarbazole (ECZ) are the photosensitizer and plasticizer, respectively. The weight percent fractions of the PATPD:DBDC:ECZ:C60 composite were 49.5:30:20:0.5%. We compared the diffraction efficiency with biplanar electrodes spaced by 100 microns at different slant angles, with interdigitated electrodes spaced by 25 microns with symmetrical incidence. It was found that the coplanar electrodes gave the best efficiency for all cases presented in Figure 4.

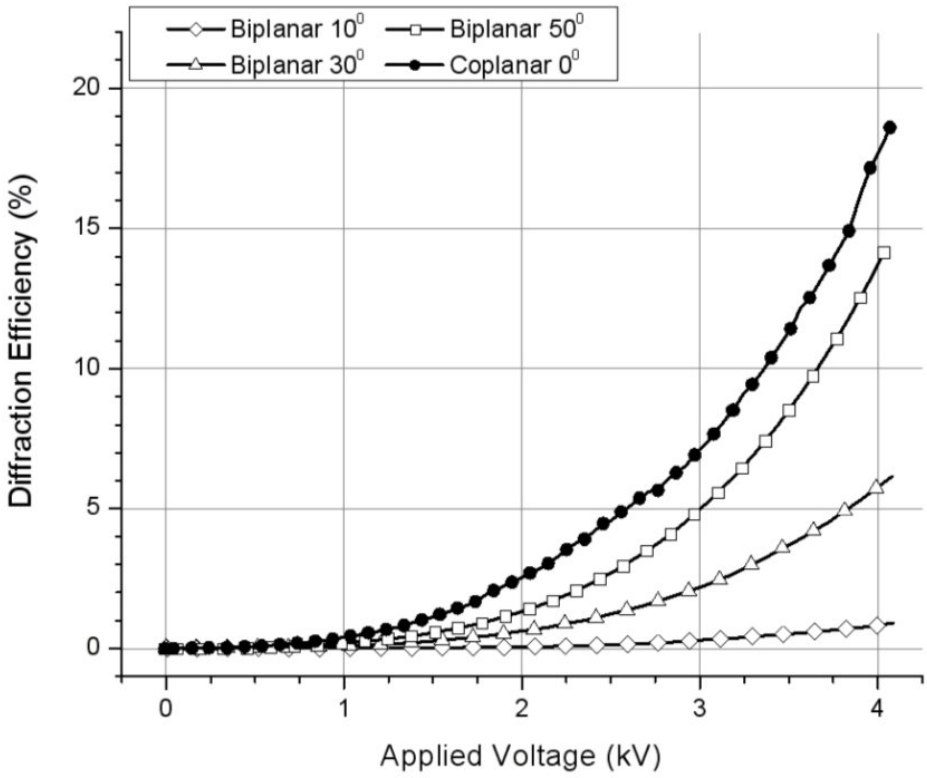

Figure 4: Diffraction efficiency according to the applied voltage. Comparison between biplanar electrodes at different slant angle and coplanar electrodes in symmetrical configuration (zero slant angle).

Another aspect of the coplanar electrodes geometry is that since the external electric field alternates direction for adjacent electrode pairs, the two beam coupling gain is reversed when the beams are moved transversely to the electrodes. Measurements supporting this are presented in Figure 5.

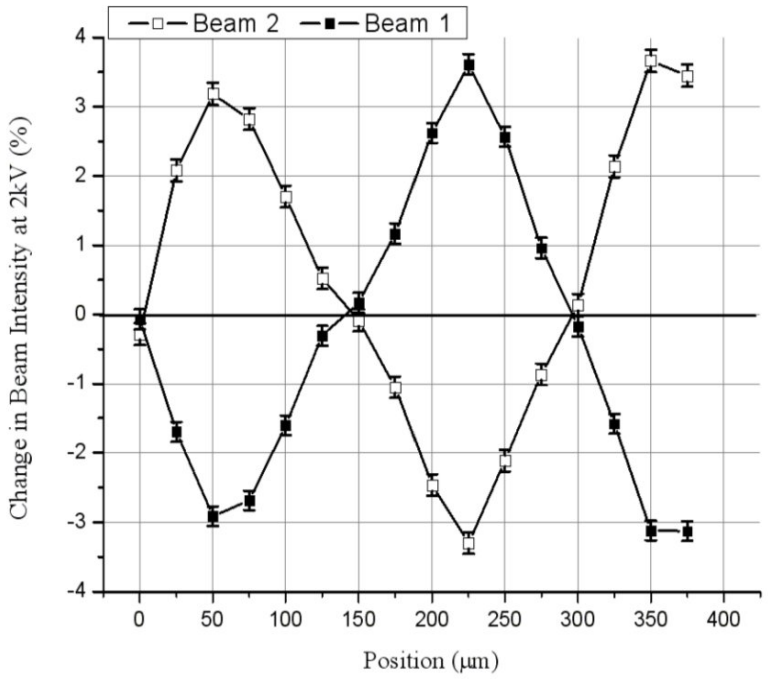

Figure 5: Two beam coupling gain measured according to the position of the beams with respect to the electrodes. Gain reversal occurs due to the field reversal every couple of electrodes.

We have made some measurement of the diffraction efficiency according to the electrode width at a constant spacing of 100 micron. Since there is no field on top of the conducting electrode, we observed a trend of the efficiency following the fill factor (Figure 6).

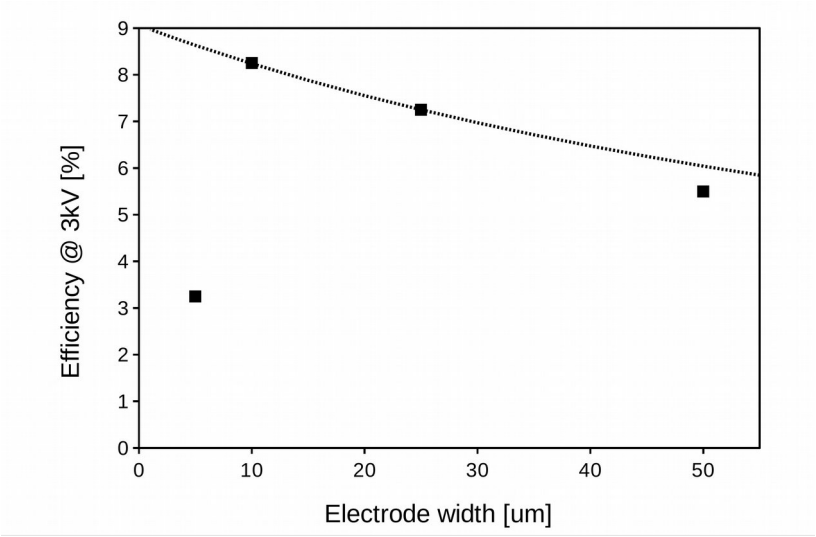

Figure 6: Diffraction efficiency according to the electrode width at constant spacing.

Results of this research have been published in: C. W. Christenson, C. Greenlee, B. Lynn, J. Thomas, P.-A. Blanche, R. Voorakaranam, P. St. Hilaire, L. J. LaComb, Jr, R. A. Norwood, M. Yamamoto, and N. Peyghambarian, "Interdigitated coplanar electrodes for enhanced sensitivity in a photorefractive polymer," *Optics Letters* **36**, 3377 (2011).

2. In situ molecular Alignment

While the applied electric field in the biplanar electrode is homogeneous, this is not the case with the coplanar electrode. Indeed, the electric field is concentrated at the edges of the electrodes and then decreases in intensity with the distance while also changing direction. This can be seen in Figure 7 where the electric field has been simulated.

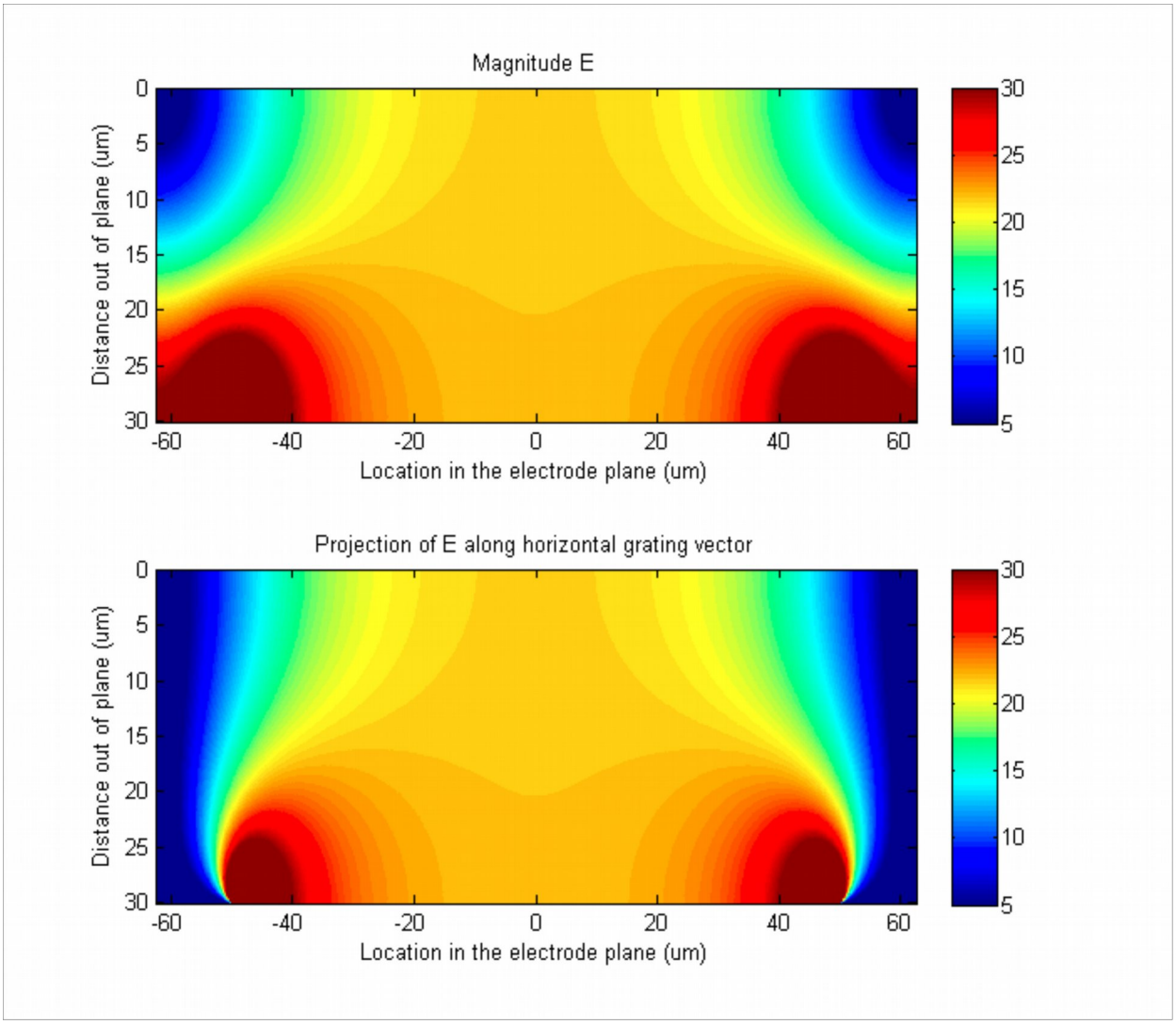

Figure 7: Simulation of the intensity of the externally applied electric field with coplanar electrodes spaced by +/- 50 um. Panel a: absolute intensity. Panel b: horizontal projection.

Since the photorefractive effect strongly depends on the intensity and projection of the external field on the grating vector, we modeled and measured *in situ* the effect of the coplanar electrodes. The measurements were carried out using EFISH (electric field induced second harmonic) and a multi photon microscope. EFISH does not probe the electric field directly but allows monitoring

of the alignment of the chromophore molecules in the field, which gives an indirect measurement of the field strength.

The setup used is presented on Figure 8. A femtosecond pulsed fiber laser emits light at 1560 nm which is focused inside the sample. The light emitted by the sample in response is collected by a microscope objective and separated by dichroic filters into the second harmonic at 780 nm and the third harmonic at 520 nm. X, Y and Z translation stages allow for scanning the sample in three axes, providing for generation of a 3D map of the emitted light.

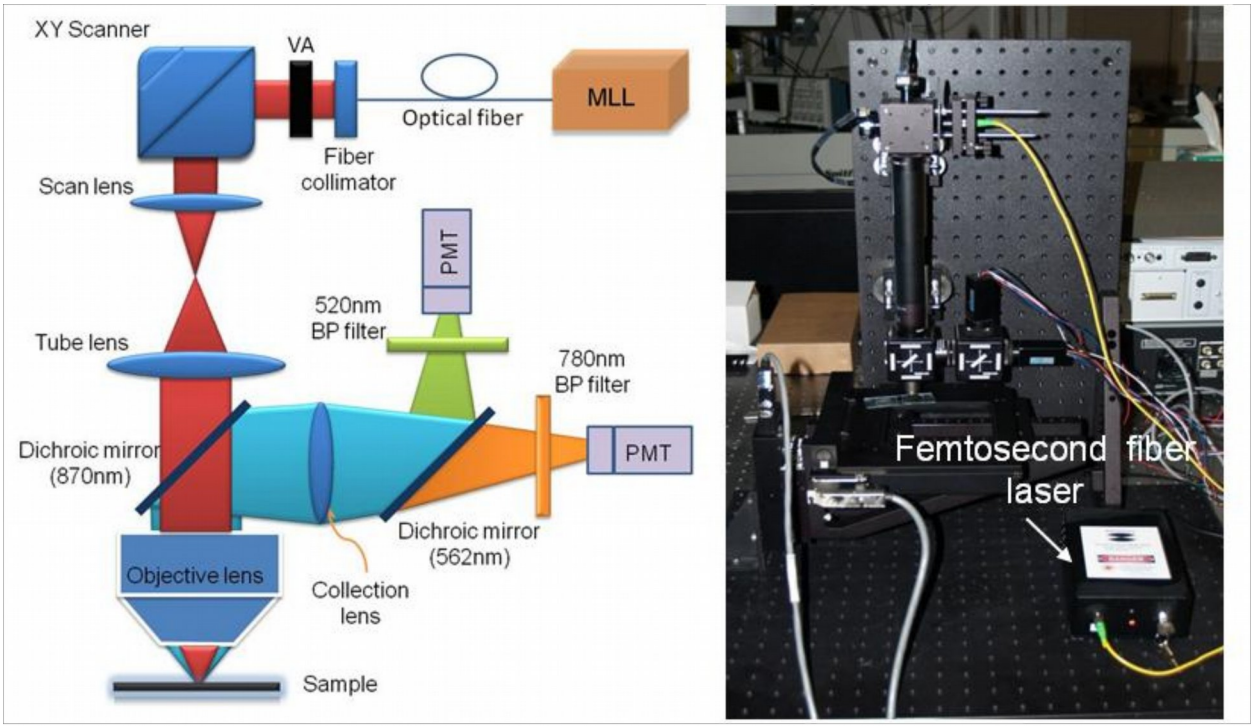

Figure 8: Multiphoton microscope setup. Schematic and picture of the actual apparatus.

Since second harmonic generation is a second order nonlinear optical process, it cannot be emitted from centrosymmetric material. So, when the chromophores are randomly oriented there is no second harmonic signal. But as soon as they start being aligned by the electric field, 780 nm light is emitted under IR illumination.

Figure 9 shows the result of the measurement on a photorefractive sample deposited on coplanar electrodes. The green signal is the third harmonic generated from the ITO electrodes. The red signal is the second harmonic generation from the chromophores where these molecules are aligned by the applied electric field.

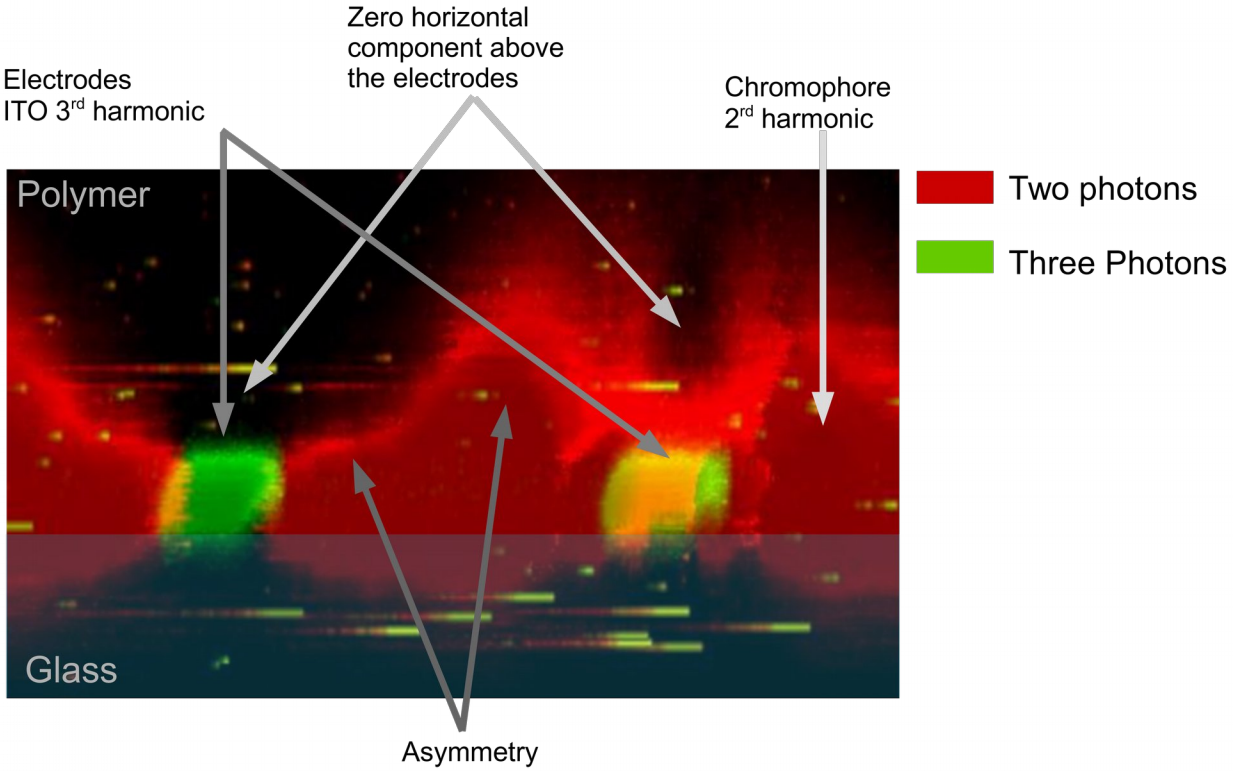

Figure 9: Multiphoton measurement of photorefractive polymer on top of coplanar electrodes.

The distinguishable features are that the field drops on the top of the electrodes since there is no field on top of conductor, and that there is an asymmetry between the positive and ground electrodes. After simulation, we found that this asymmetry is caused by the charge mobility inside the material, as it can be seen in Figure 10.

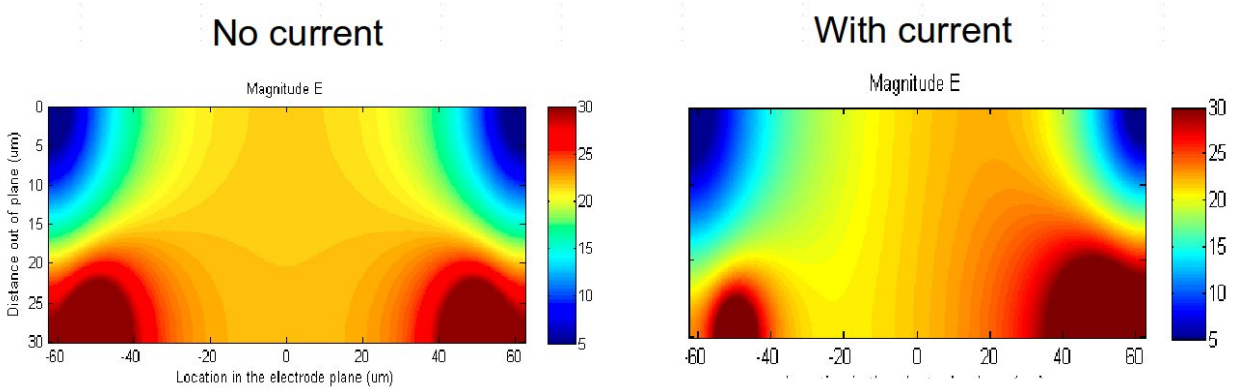

Figure 10: Intensity of the electric field generated by coplanar electrodes without conduction, and with conduction inside the sample.

Dynamic models of photorefractivity in polymers have long been used to direct the formulation of new and more efficient PR devices. Ostroverkhova modified the Schildkraut and Buettner model describing the relationship between material parameters and electric fields and their contribution to the PR response. The response depends on a variety of material parameters such

as sensitizer densities and trap levels, but in this case the focus is on the effect of the electric field dependent parameters. These are the photogeneration cross-section (σ), hole drift mobility (μ), trapping (γ) and recombination (γT) rates with field dependences on either the magnitude of the applied field or the projection of the field onto the grating vector. Using the electric field model to evaluate these parameters across the electrodes, the resulting space-charge field was used to calculate the refractive index modulation.

The decrease in electric field with increasing distance from the electrodes leads to a refractive index modulation whose magnitude is an order of magnitude higher near the edges of the electrodes than in the remaining bulk of the material, affecting the diffraction of the reading beam. Computational propagation of the reconstructed beam through the grating was performed using the Crank-Nicholson method. Implementation of periodic boundary conditions took advantage of the repeating nature of the electrode structure. Figure 11 (a) shows the results of propagation through the PR polymer across one period of the electrode structure. The effect of the spatially inhomogeneous electric field is to concentrate diffraction of the reconstructed beam near the electrode edges, which affects the resulting beam uniformity in a high spatial frequency manner. Tilting the writing beams with respect to the normal to the sample plane increases the number of these high index regions that the reconstruct beam encounters. For a range of tilt angles from 0 to 20 degrees, the peak power to RMS ratio decreases by 15%, indicating an increase in the spatial homogeneity of the reconstructed beam with increasing tilt angle. Figure 11 (b) shows the propagation results of the full width of the reading beam in the output plane. The presence of side lobes is due to diffraction from the underlying low spatial frequency refractive index modulation from the periodicity of the applied electric field. With increasing tilt angle, the diffracted order that is closer to the sample normal than the reconstructed Bragg angle (left peak) is less efficiently diffracted by the base structure due to its increasing Bragg mismatch.

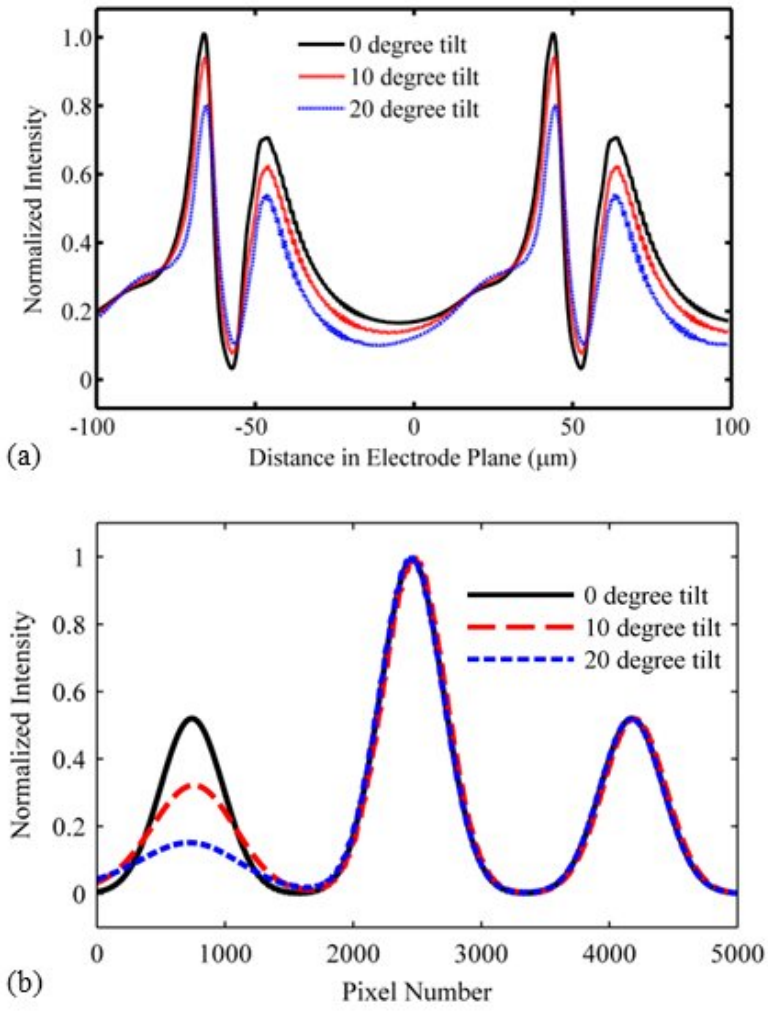

Figure 11: Propagated reconstructed beam at 0, 10, and 20 degree tilt angle geometries of the recording beams in (a) electrode and (b) full beam scales.

Experimental verification of the applicability of these adjusted models in device design was executed. Non-degenerate four-wave mixing measurements were performed in which a grating was formed by two 532 nm mutually coherent beams with an inter-beam angle of 30°. The orientation of the coplanar electrodes was such that the resulting fringes were parallel to the electrode 'fingers', ensuring that the generated charges traveled across the fringes to become trapped instead of along them. A 633 nm reading beam counter-propagating at the appropriate angle accounting for the wavelength mismatch diffracted from the grating and was monitored by a CMOS detector for 0, 10, and 20 degree tilt angles. Figure 12(a) shows the original and diffracted beam profiles taken in a cross-section perpendicular to the plane of diffraction. As expected, there was no significant change in the profile of the beam since this is the direction along the fringes and perpendicular to the underlying electrode index modulation. Figure 12(b) is

a cross section in the plane of the electrode index modulation and multiple orders flanking the primary diffracted beam are present. Additionally, the decrease in the intensity of the left order follows that of the theoretical model (Figure 11(b)). The fine structure inhomogeneity from the micron-scale diffraction analysis is seen in the ±1 orders but is insignificant on the magnitude of the full diffracted beam. This indicates that there is an intensity threshold above which the non-uniformity due to the spatial electric field modulation is negligible.

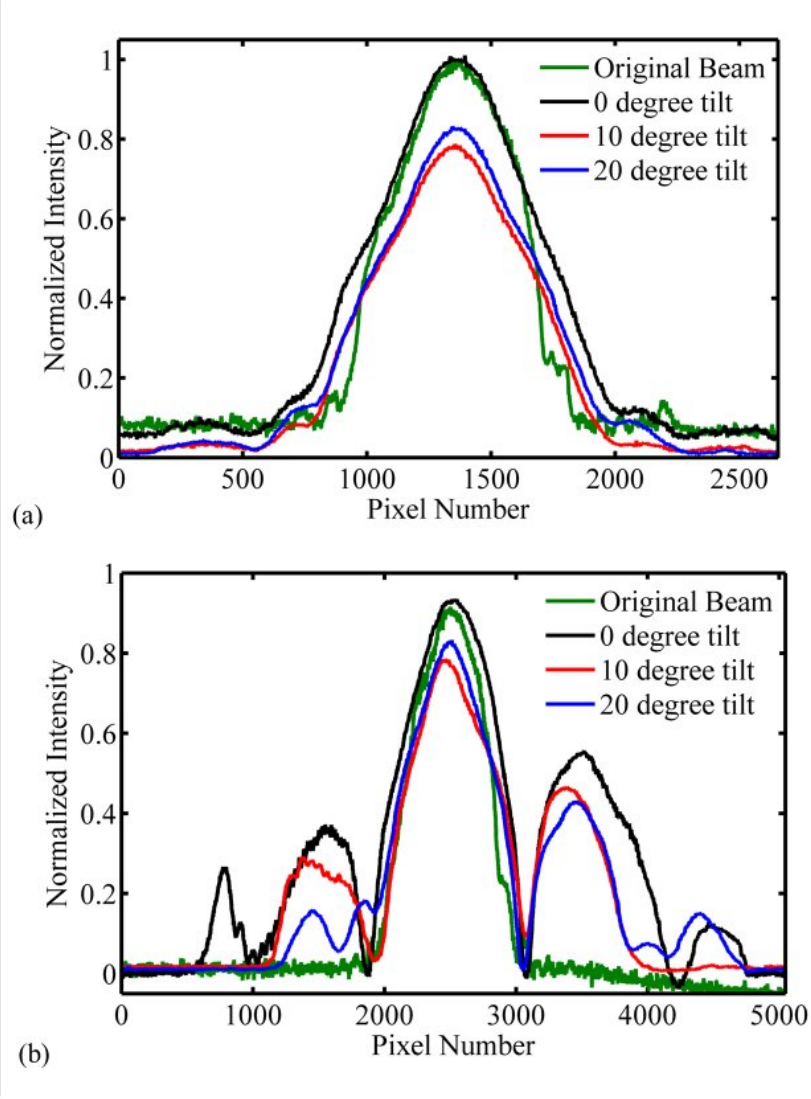

Figure 12: Cross-sections of the measured incident and diffracted beam profiles taken (a) out of the plane of diffraction and (b) in the plane of diffraction for various tilt angles.

Results of this research have been published in: B. Lynn et al., "Real-time imaging of chromophore alignment in photorefractive polymer devices through multiphoton microscopy" accepted for publication in *MRS Communication*, 2015.

3. Charge species characterization

This research has been done in collaboration with Dean Evan's team at AFRL.

A recent advancement in PR polymer devices is the application of thin inert buffer layers between the electrodes (ITO) and the PR polymer such as APC (amorphous polycarbonate). The thin buffer layers enable the application of higher applied electric fields (> 70 V/μm) for longer periods of time by limiting electronic avalanche that causes excessive currents leading to dielectric breakdown in the polymer. Although large applied fields can potentially be used to improve the amplitude and phase-shift of the index grating, it has also been observed that competing (electrons) PR gratings can be created by the presence of oppositely charged carriers.

To characterize the formation of the PR gratings in the polymer, for both the transient and steady states, self-pumped two-beam coupling was used. The time dynamics is monitored by subjecting the polymer to the laser light before the applied electric field, which allowed us to measure chromophore reorientation in addition to grating formation. Figure 13 shows the time dynamics for the change in normalized transmission for both 532 nm and 633 nm as a result of two-beam coupling in the reflection geometry. The temporal behavior of the transmission changes dramatically for 532 nm excitation when applying fields at and above 70 V/μm; a similar behavior is observed for lower applied fields (35 V/μm) for the 633 nm wavelength. Initially, there is a steep decrease of the transmission due to chromophore reorientation and the formation of the hole grating, which is followed by a small increase in transmission due to the formation of the electron grating (i.e. the competing grating). At $t \approx 40$ s (for the case of 532 nm light) there is a further decrease in the transmission.

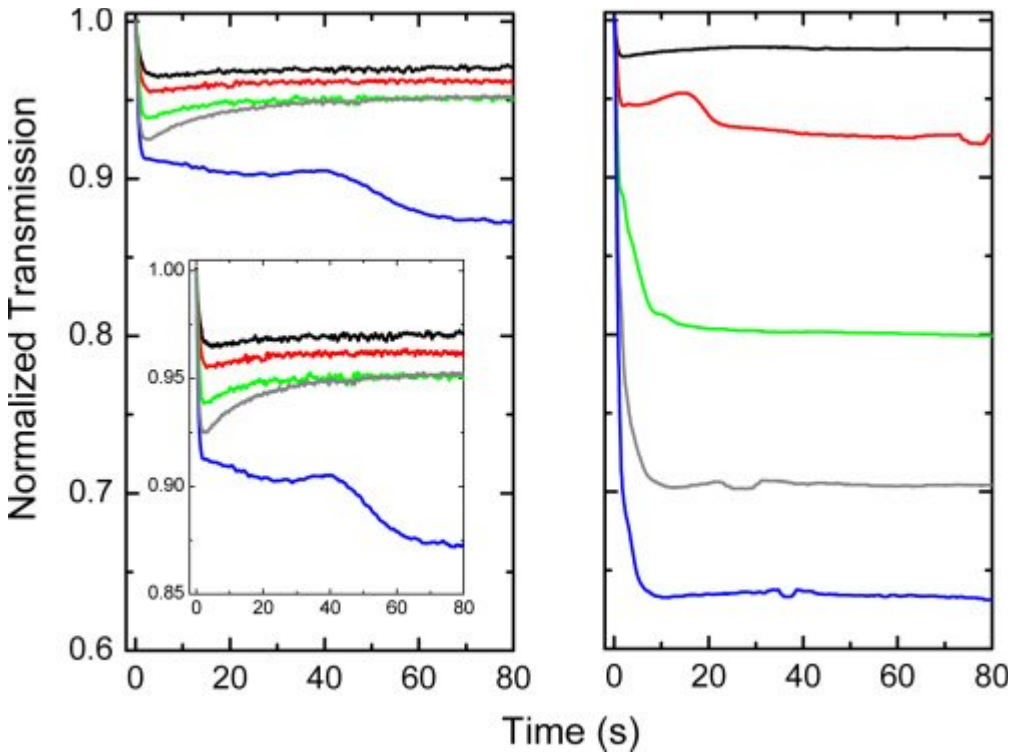

Figure 13: Time dynamics of the grating formation using (left) 532 nm and (right) 633 nm light to record the gratings as a function of applied fields: in order from top to bottom - (black) 30 V/μm, (red) 40 V/μm, (green) 50 V/μm, (gray) 60 V/μm, and (blue) 70 V/μm.

A comparison of the two-beam coupling efficiency in terms of the change in optical density, ΔOD, for the steady state as a function of the applied electric field, is shown in Figure 14. ΔOD is defined as $\log(T_0/T)$; T_0 and T are the transmission values before and after the formation of the PR grating, respectively. Figure 14 shows the increase of the two-beam coupling efficiency due to gain enhancement (beyond the regime of the electronic contribution to the PR grating), which is observed with large applied fields using 532 nm light and moderate applied fields using 633 nm light. The decrease in the applied field required for the enhanced ΔOD observed at 633 nm is explained by the increased absorption compensated photocurrent.

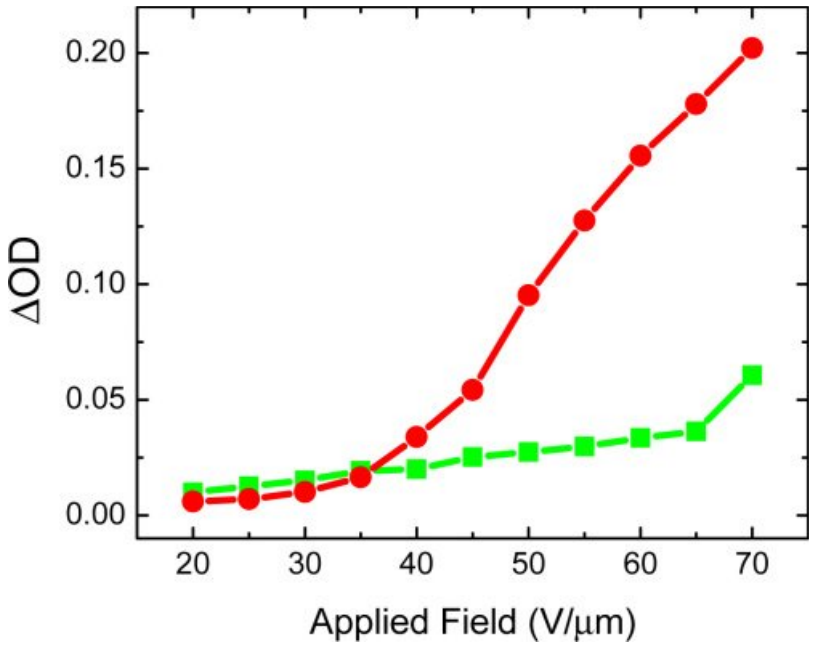

Figure 14: Change in beam coupling efficiency (in terms of change in optical density, ΔOD) as a function of the applied electric field using 532 nm (green squares/line) and 633 nm (red circles/line) light. Note the threshold voltages for the onset of the nonlinear gain enhancement: ≈40 V/μm using 633 nm recording light and ≈70 V/μm using 532 nm recording light

There are a few possible scenarios that can be proposed to explain the gain enhancement beyond the regime of competing gratings; these include contributions from either positive charges or positive ions. The increased gain can be attributed to an additional charge species that is capable of forming a space-charge field present in the PR polymer, e.g. holes, electrons, ions. Regardless of the source, the two-beam coupling data shows that the gain enhancement complements the initial hole-formed grating, so electrons or negative ions contributions can be ruled out. If the buildup dynamics of the enhanced component of the grating formation is the same as the dynamics of the initial hole-formed grating, one can postulate that holes are involved; if the enhancement is significantly slower than the initial hole-formed grating response time, then positive ions would likely be the responsible source. To determine if the source of the gain enhancement is holes or positive ions, exponential fits can be used to determine the relative amplitudes and formation times of individual components of a diffraction grating formed under many conditions. The dynamics of the grating formation are indeed the same for the initial hole-formed grating and the enhanced gain region, which indicates that the species are indeed holes and positive ions can be ruled out.

The presence of additional charge species has a considerable effect on the two-beam coupling strength of PR polymers. It has previously been shown that when competing charge species are present, the two-beam coupling strength is decreased. This is because at moderately high applied

fields electrons are mobile and become trapped, forming a competing space-charge field which reduces two-beam coupling gain and diffraction efficiency. But here, for both 532 nm and 633 nm, nonlinear enhancement of the PR gain can be achieved by applying higher external fields. These larger fields allow for high electron mobilities (with respect to hole mobilities), which then do not contribute to competing grating formation. The mobile electrons contribute to increased conductivity, explaining why the polymers suffer dielectric breakdown under large bias fields. Due to reduced absorption at 633 nm, all observed transient effects occur at lower bias fields as compared to 532 nm.

Results of this research have been published in: C. Liebig et al. "Achieving enhanced gain in photorefractive polymers by eliminating electron contributions using large bias fields," *Optics Express* **21** (25), pp 30392-30400 (2013).

4. New materials

Functionalized Reduced Graphene Oxide

Prior studies have been performed on the use of graphene additives to enhance the performance of photorefractive polymers. Grishina et. al. (*High Energ. Chem.* **47**(2), 46–52 (2013)) doped a PVK based polymer composite with 0.15 wt% graphene, intended as a photo-sensitizer for use at 1064nm. Graphene absorbs nearly uniformly across the visible and near infra-red range and once excited, the resulting charges are highly conductive across the conjugated sheet. The form of graphene in this study was flakes of three to four monolayers which, while yielding unity quantum excitation efficiency, led to a significant degree of scattering due to the large particle size and, consequently, negligible gain was measured. Thomas et. al. (*J. Mater. Chem. C* **2**, 7639-7647 (2014)) doped the same system that we use with graphene as a substitute for PCBM in an attempt to increase sensitization. They also had a problem with scattering so reduced the loading to 0.03wt% from the standard 0.5wt% PCBM loading for these materials. In doing so they found a larger and faster diffraction than a similarly 0.03wt% doped PCBM composite, but the low doping required the application of nearly 1W/cm^2 of recording energy.

Figure 15 - Octadevylamine functionalized reduced graphene oxide (ODA-rGO)

Functionalizing small molecules with long chain pendant groups is well known to increase solubility in solutions and compounds, decreasing the energetic favorability of stacking and agglomeration. Additionally, reduction of the graphene sheets increases dispersability while having no effect on opto-electronic properties in the visible wavelength regime. We used octadecylamine functionalized – reduced graphene oxide (ODA-rGO) in the following study, the molecular structure of which is illustrated in Figure 15. Also shown is the ODA-rGO in solution, indicating a large degree of solubility in chloroform. Instead of substituting graphene for PCBM, we chose instead to add it to the standard composite to enhance its performance. Due to the

energetics of the PR polymer system, ODA-rGO is expected to create a charge-transfer complex with the chromophore, increasing the quantum yield of the chromophore and resulting in an increase in the number of effective sensitizers. This charge-transfer complex should also aid in quenching fluorescence of the chromophore during the recording stage by introducing a more favorable avenue to relaxation, an important feature for display applications.

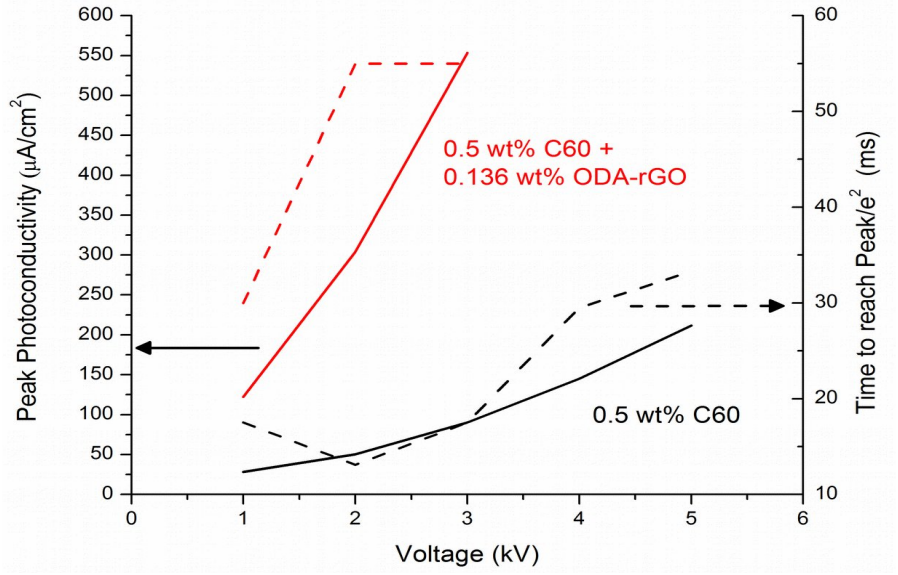

Figure 16: Peak photoconductivity (left axis, solid line) and time to reach 1/e2 value (right axis, dashed line) for the C60 sensitized (black) and the C60+ODA-rGO sensitized compositions as a function of applied voltage across 100μm films.

Photoconductivity results shown in Figure 16 indicate that the addition of 0.15wt% ODA-rGO to the 0.5wt% C_{60} system increases the photoconductivity of the device under illumination as expected. The right axis shows the time to reach the $1/e^2$ point of maximum and while it takes longer for the co-doped system, the slope of the rise is faster for the co-doped system, as shown in Figure 17. While this indicates a factor of two improvement in the photo-electric performance, the 0.15wt% loading samples still had some trouble with agglomeration of species as indicated by a maximum voltage of 30V/μm prior to dielectric breakdown. In order to continue with this line of research, we propose changing the functional group to one that is more specifically optimized for the compounds in our photorefractive polymer devices. This will allow the loading of rGO at levels that could provide significant performance improvement while reducing the agglomeration still seen with ODA functionalization.

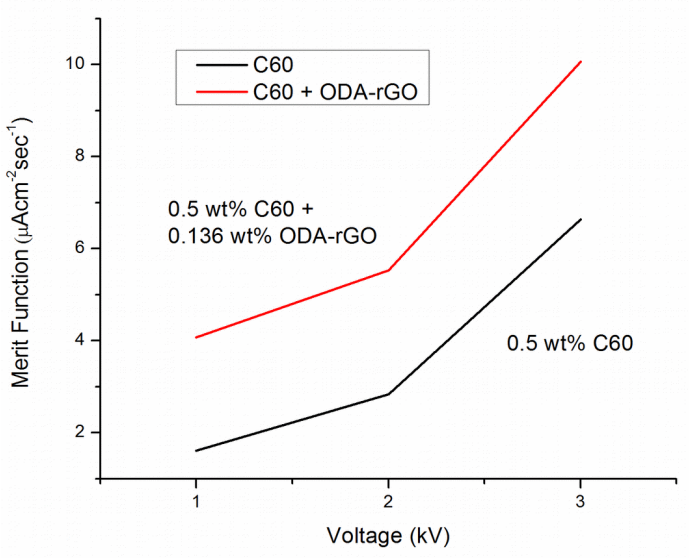

Figure 17 – Merit function of standard C_{60} based system compared to that of the ODA-rGO co-doped system defined as the time to rise for peak photoconductivity normalized by the magnitude of the conductivity. Displayed as a function of voltage applied across 100μm films.

Sensitization by Perylene Diimides

Prior studies have been performed using perylene compounds as sensitizing agents in photorefractive polymers. Denz, Wang, et. al. (*Adv. Mater.* **24**(16), 2104–2108 (2012)) used C12-perylene bisimide (PBI), and C12-di-perylene bisimide (DiPBI) as sensitizer replacements for PCBM in a PVK/5CB system. The 0.034 mol% DiPBI system exhibited a doubling in gain to 188cm^{-1} over the 0.136 mol% PCBM doped polymer at 70V/μm as well as a 40x increase in the speed of the response. This indicates a promising system although no four-wave mixing results were published. Denz, Wang, et. al. Denz, Wang et al. (*Opt. Mater. Express* **2**(6), 856–863 (2012)) also investigated the use of DiPBI in a TPD:polystyrene system but this analysis was only performed at low voltages, generally not in the range of use for diffractive based systems. They found that 0.02 wt% loading of DiPBI in the TPD:PS system led to a 10x higher photoconductivity but an associated 2x decrease in the gain compared to the previously mentioned PVK system.

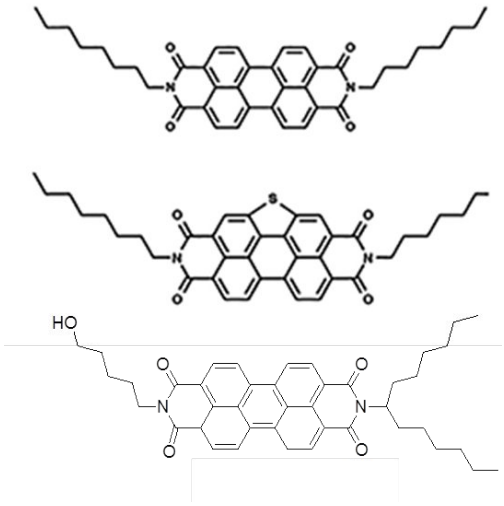

Figure 18 - Perylene diimides. Di-C8-PDI (top), Di-thio-C8-PDI (center) and DiOH-C8-PDI (bottom).

We used perylene diimides (PDIs) as replacements for PCBM in our PATPD: 7-DCST: ECZ: PCBM system. We had three different functionalized molecules available, illustrated in Figure 18, with the Di-C8-PDI and Di-thio-C8-PDI synthesized by Dr. Balakrishnan in our group and the Di-OH-C8-PDI (Pery-OH) provided by Dr. Ziolo at Centro de Investigacion en Quimica Aplicada. Figure 19 shows absorbance measurements of the three sensitizers compared to the standard PCBM sensitized polymer composite as well as an unsensitized version.

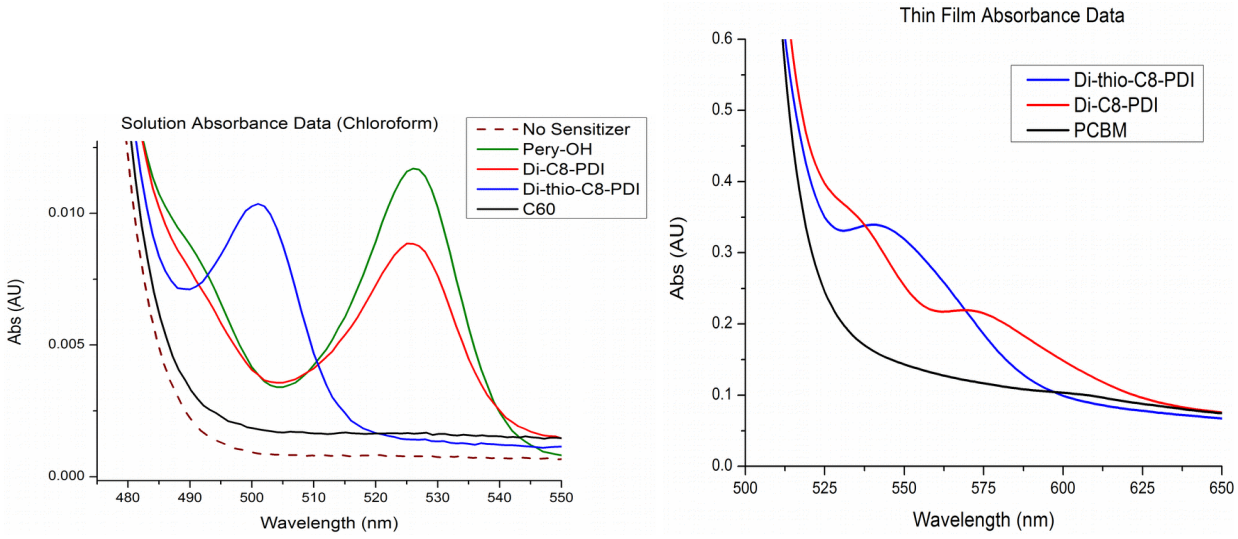

Figure 19 – (left) Solution absorbance data for various photorefractive polymer solutions in chloroform. (right) Thin film absorbance data for various sensitizers integrated into the PR polymer. All sensitized solutions have 0.5wt% loading of the sensitizer molecule.

Preliminary solutions were made using Di-C8-PDI with an initial loading of 0.5wt% but a significant quantity of the Di-C8-PDI crystallized and was lost in the filtering process, resulting

in an unknown concentration. The results shown in Figure 20 show a mild increase in photoconductivity at lower voltages and an increase in speed across the entire range. The photoconductivity normalized for speed is shown in Figure 21 and indicates a constant slope of photoconductive speed above 3kV. Subsequent samples of D9-C8-PDI and Pery-OH were made with 0.5wt% loading using a different filtering method in order to test the response of a known loading but this loading was too high, as the sensitizer caused rapid crystallization in the composite. 0.25wt% polymer composite was mixed and does not show visible crystallization.

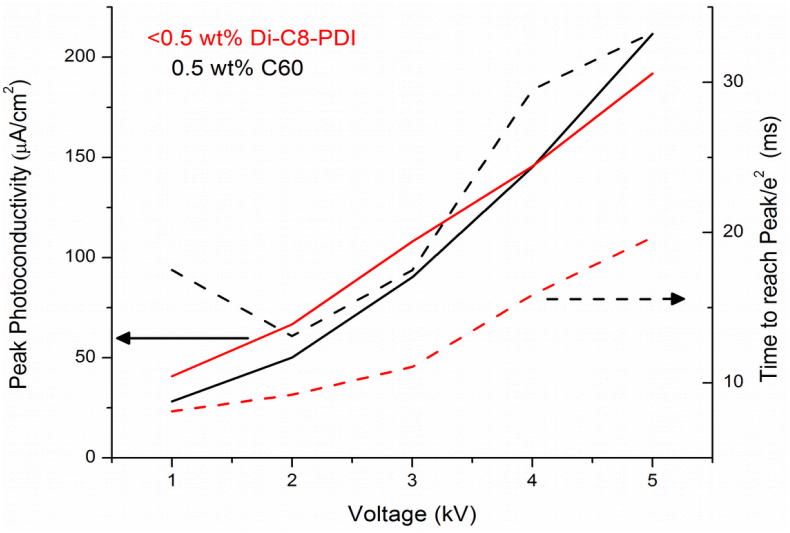

Figure 20 – Peak photoconductivity (left axis, solid line) and time to reach $1/e^2$ value (right axis, dashed line) for the C_{60} sensitized (black) and the Di-C8-PDI sensitized compositions as a function of applied voltage across 100μm films.

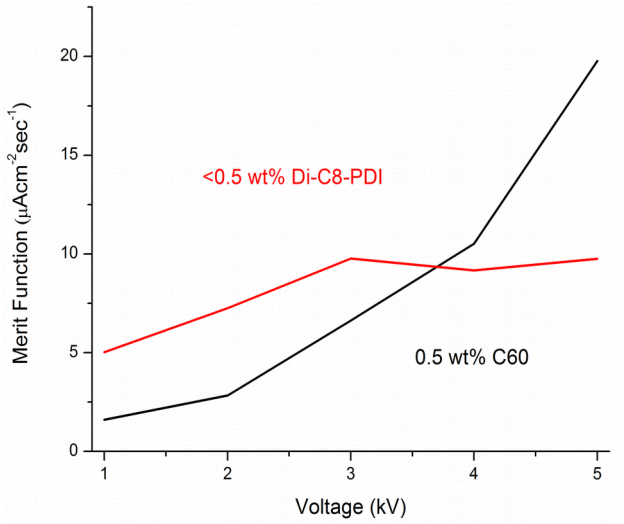

Figure 21 - Merit function of standard C_{60} based system compared to that of the Di-C8-PDI doped system defined as the time to rise for peak photoconductivity normalized by the magnitude of the conductivity. Displayed as a function of voltage applied across 100μm films.

Other sensitizers

Additional sensitizers were provided by Dr. Ziolo at Centro de Investigacion en Quimica Aplicada, Fe5PPV and $3BzC_{60}$, with molecules illustrated in Figure 22. Absorbance data indicated that these sensitizers were not expected to exhibit significant increases in quantum efficiency and they were not soluble in the PR compounds to any significant degree, causing crystallization at even 0.05wt% loadings.

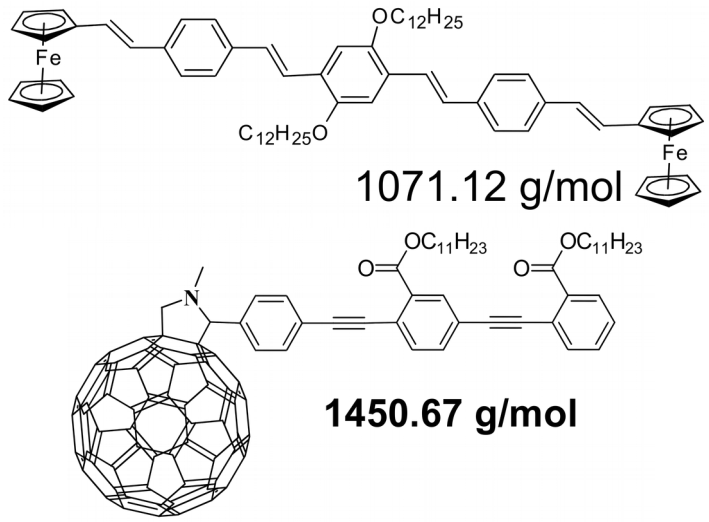

Figure 22 – (top) Fe5PPV and (bottom) $3BzC_{60}$ molecular structures and molar weights

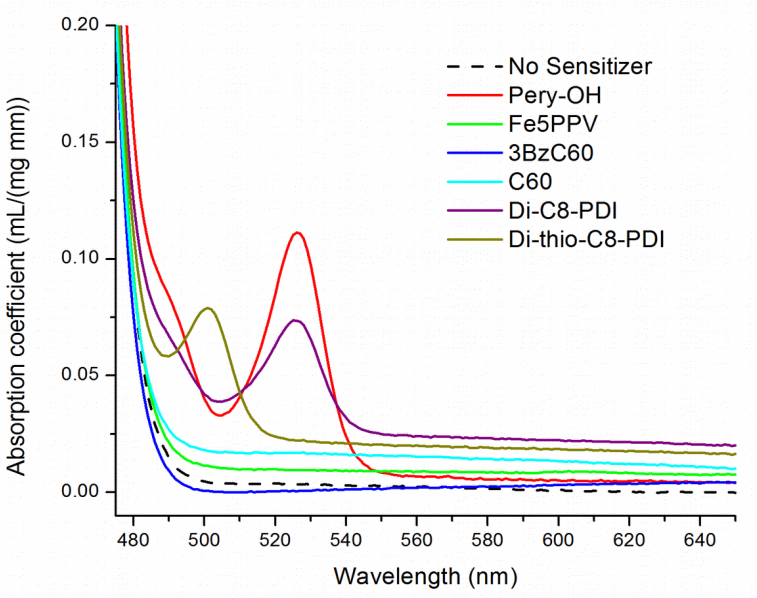

Figure 23 – Absorption coefficient of various sensitizers in PR composite solution

Significant results of this research have been published in: B. Lynn et al., "Photorefractive polymer for holography", review article, *Journal of Polymer Science Part B: Polymer Physics* **52**, pp 193-231 (2013) (November 2013).

5. Direct fringe writing

This work has been done in collaboration with Prof. Bove's group at MIT.

The architecture for direct writing of holographic fringes in photorefractive materials encompasses fringe computation, display on spatial light modulators, optical projection and demagnification for transfer to the material, and spatial multiplexing for large-image recording. An overview of the system process is depicted in figure 24.

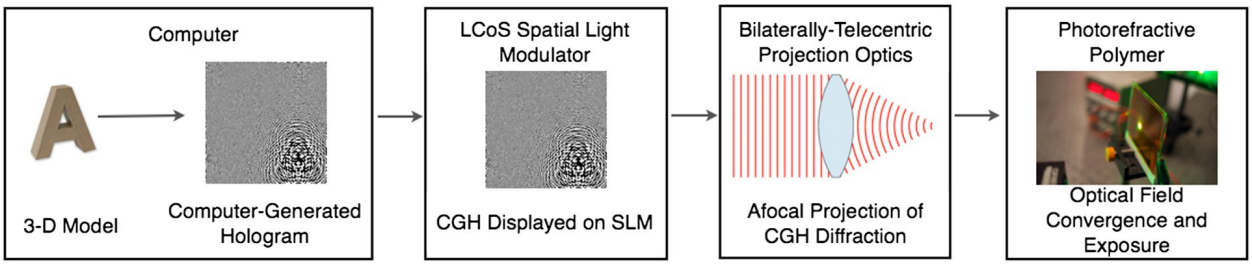

Figure 24: System overview for direct optical fringe writing in photorefractive polymer.

The fringe computation used for this study has been performed using the Reconfigurable Image Projection (RIP) hologram algorithm which was originally developed at the MIT Media Lab for video-rate, horizontal parallax-only (HPO) fringe pattern generation

Direct writing of holographic fringes into the PRP material involves demagnification and transfer of the fringe pattern displayed on a spatial light modulator. A CW beam from a DPSS laser at λ = 532 nm is beam-expanded and collimated. This beam illuminates a liquid-crystal-on-silicon (LCoS) modulator displaying the information corresponding to an elemental fringe pattern. The LCoS module, used in the current study, has been furnished by Silicon Micro Display, has an 8.5 µm pixel pitch and 1920×1080 resolution. A polarizing beam-splitter (PBS) is used to operate the LCoS module in an amplitude modulation configuration. The modulated light is then projected into the PRP material by means of a bilaterally telecentric optical system comprised of two cylindrical singlet lenses in a Keplerian telescope configuration. The focal length of the input objective L1 is f1 = 250 mm and the focal length of the output objective L2 is f2 = 50 mm. This configuration yields a demagnification of 5×. Given the 8.5 µm pixel dimension of the SLM and the 5× demagnification specified by the telescoping optics, the nominal smallest pixel dimension in the optical irradiance distribution arriving at the PRP is 1.7 µm.

In order to validate the direct fringe writing architecture and to measure diffraction efficiency, a sinusoidal grating was displayed on the SLM and transferred to the PRP sample using an irradiance of 150 mW/cm^2, exposure time of 5 s, and PRP applied voltage of 5.5 kV. Upon readout with a beam from a helium-neon laser at λ = 632.8 nm, a measured first-order diffraction efficiency of 12 percent was observed.

Horizontal parallax only holographic fringes of a teacup model were computed using the RIP algorithm and transferred to the PRP sample. After total hologram rastering, the resulting

holographic image upon readout with beam-expanded and collimated light from a helium-neon laser at λ = 632.8 nm is depicted in Figure 25. Note that this image exhibits much higher brightness (diffraction efficiency), longer persistence, better discriminability, and better apparent depth upon reconstruction relative to previous images generated through our direct fringe transfer architecture. However, discrimination of fine features is difficult due to the presence of noise and other artifacts. Because the optical system used for imaging the CGH pattern from the SLM to the PRP is not optimized for high imaged contrast and minimal aberrations, anomalous diffraction due to imperfect imaging is likely a contributing factor in the low contrast in the three-dimensional reconstruction and the large amounts of noise.

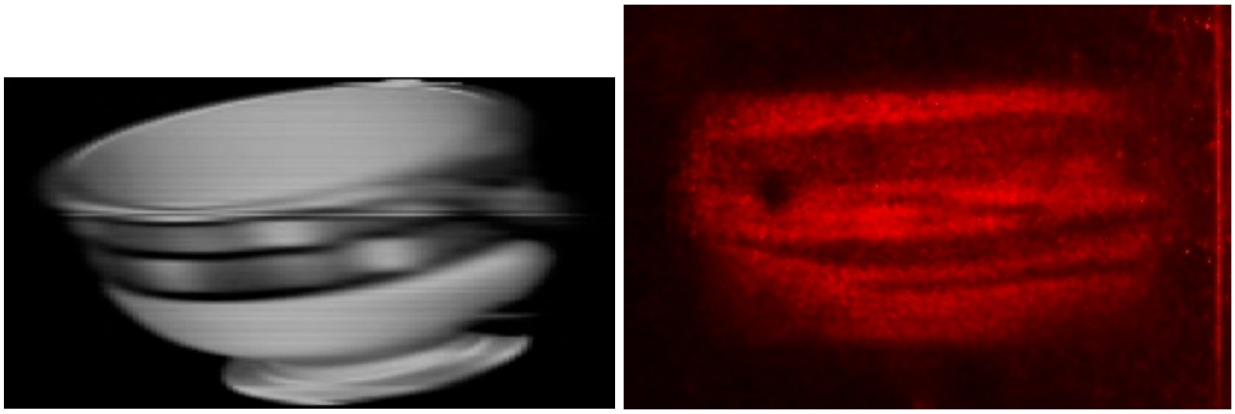

Figure 25: Model and holographic image of the computer-generated teacup.

Results of this research have been published in: S. Jolly et al., "Direct fringe writing architecture for photorefractive polymer-based holographic displays: analysis and implementation", *O*pt. Eng. **52**(5), 055801 (May 07, 2013).

6. Pulse width response

For conventional holographic materials, such a silver halide and photopolymers, the diffraction efficiency response is invariant with the pulse width of the writing laser and only depends on pulse energy. However at very small pulse temporal width and large peak power, this law breaks down, a phenomenon that is known as the “reciprocity failure”. We observed a similar behavior for photorefractive polymers when using a nanosecond pulse laser compared to CW recording. During this program, we carried on a study of the diffraction efficiency according to the temporal pulse width of the writing beams over 9 orders of magnitude, and linked the observation to the PR mechanism.

To do so, we built a specific laser source which pulse width can be tuned. We used a MOPA configuration (master oscillator power amplification), where a CW IR telecom diode laser is chopped into pulses by a Pockels cell. The pulses are then re-amplified outside the cavity by two diode pumped fiber amplifiers. The IR pulse is then converted into 532 nm with a frequency doubling crystal and injected into a four wave mixing setup to record a diffraction grating into the sample. To be sure the grating is recorded with one single pulse, another Pockels cell is used to trigger a temporal window. A 633nm HeNe laser is used to read the grating and to measure the diffraction efficiency.

The pulsed fiber laser characteristics are:

- Energy per pulse: up to 100 µJ/pulse
- Pulse temporal width: from 250 ns to 250 µs
- Repetition rate: up to 10kHz
- Coherence length: 1cm

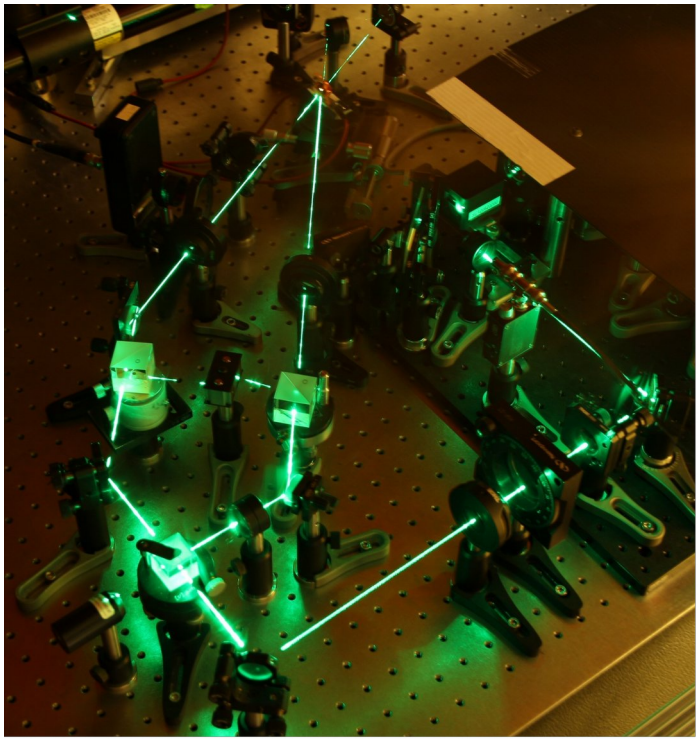

Figure 26: Four wave mixing setup fed by the fiber laser.

Three primary time-dependent phenomena contribute to the development of a refractive index grating. The first is the photogeneration of charges in response to the incident illumination. This process takes on the order of picoseconds and as this is three orders of magnitude faster than a nanosecond pulse, it is therefore not a process that will be significantly affected by the pulse lengths that are under investigation here. On the other hand, this effect is highly intensity dependent and will play a large role in the relationship between the magnitude of the diffraction efficiency and the pulse energy. Additionally, the photogeneration efficiency is electric field dependent which leads to an expected difference in performance between the buffered and un-buffered devices. The second step is the transport and trapping of the now excited charge carriers, with characteristic times on the order of 0.1-5ms, well within the range of pulse width interest. These processes are highly field dependent and are also expected to play a role in the buffer/no buffer comparison. The final step is chromophore orientation to the space-charge field, taking on the order of 0.1 to 1ms, again on the scale of interest and again a highly field dependent effect.

The use of three different lasers enabled measurements of the PR polymer response to pulse width and energy from 6ns to 1sec, covering nine orders of magnitude. The shortest time scale measurements were performed using a 6ns 532nm InnoLas SpitLight laser with single pulse capabilities and energies ranging up to 200mJ per pulse. The longer time scale pulses were created using a 532nm Coherent Verdi V18, a single longitudinal mode CW optically pumped

semiconductor laser with a max power of 18W. The beam was externally modulated using an AOM to create single pulses with widths ranging from 1.5ms to 1s.

Four-wave mixing measurements were performed on AS-J2 samples with a single 10µm APC (amorphous polycarbonate) buffer layer in order to characterize the current state-of-the-art device across a range of pulse energies, from 10mJ/cm^2 to 30mJ/cm^2 and across the entire range of pulse widths. The results are shown in Figure 27, displayed in log scale to show the microsecond pulse width regime clearly.

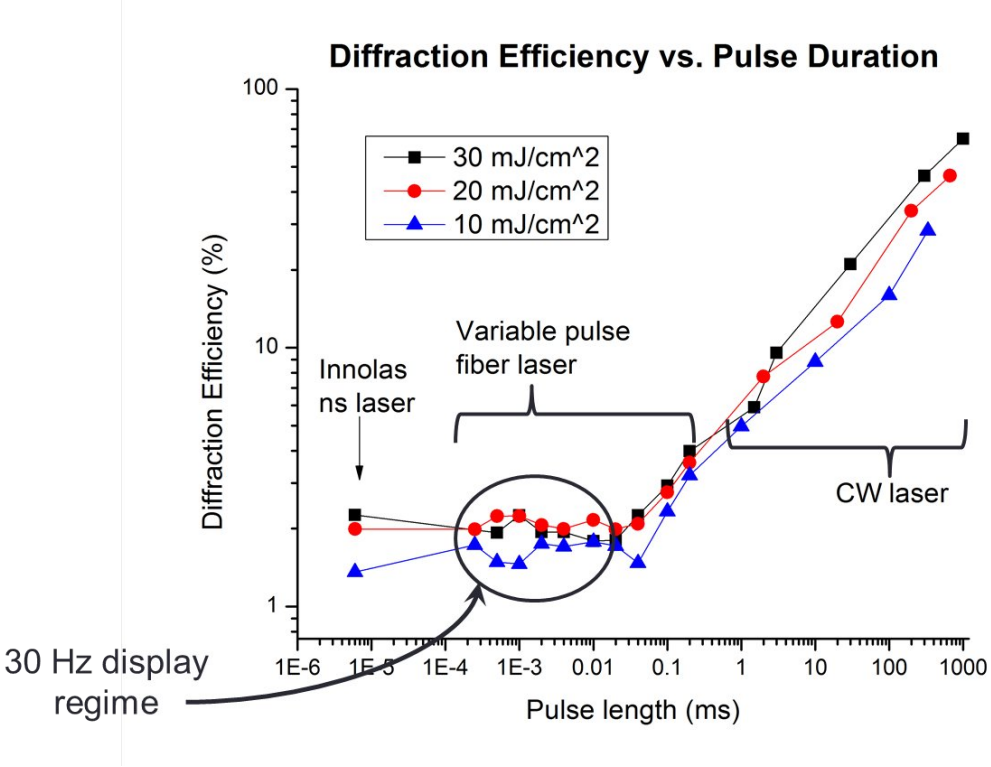

Figure 27: Diffraction efficiency vs. pulse width for a range of pulse energies on samples with a 10µm APC buffer layer.

For longer pulse lengths, depicted by the linearly decreasing region on the plot, the decrease in diffraction efficiency is due to a combination of photoelectric, orientational and diffractive effects. The process of grating formation in photorefractive polymers begins with absorption of the interfering pulses in the bright regions of the fringes. The rate of space-charge field formation at a constant external bias depends on the number of excited charge carriers. As the energy per pulse is decreased for constant pulse width, the number of mobile charge carriers decreases, correlating to a decrease in the space charge field and refractive index modulation. These result in the reduction in diffraction efficiency with decreasing pulse energy, as seen in Figure 28.

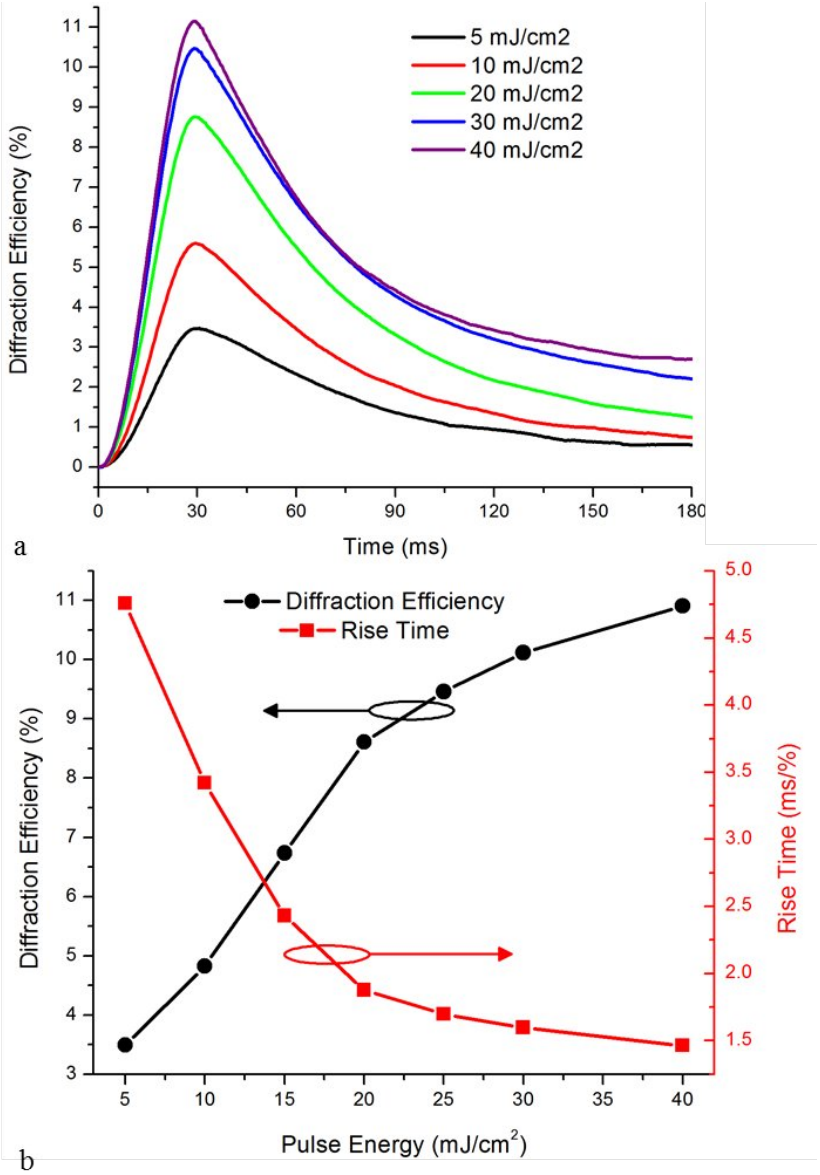

Figure 28: 10µs pulse length FWM results of AS-J2 (no buffer) showing a) diffraction grating growth and decay dynamics for various pulse energies and b) peak diffraction efficiency and rise time in units of ms/% diffraction efficiency.

At constant pulse energy, longer pulses expose the material with a lower instantaneous flux, but the exposure time is longer, with continuous illumination supporting multiple excitation/transport/absorption events for each charge carrier until it reaches a dark fringe. As the illumination time decreases below the threshold necessary for transport across the fringe spacing, the charge distribution is no longer sinusoidal in form. The duty cycle of the space-charge field begins to decrease, while the peak-to-peak value increases due to the smaller separation of the same quantity of charges. Figure 29 illustrates the extreme case in this scenario in which only a

single excitation/transport/absorption event occurs and the duty cycle of the resulting refractive index modulation is significantly less than the optimal 0.5. The right side of Figure 29 illustrates the effect that this duty cycle change has on the efficiency of diffraction from the grating itself, following a $\sin^2(duty\,cycle)$ relation.

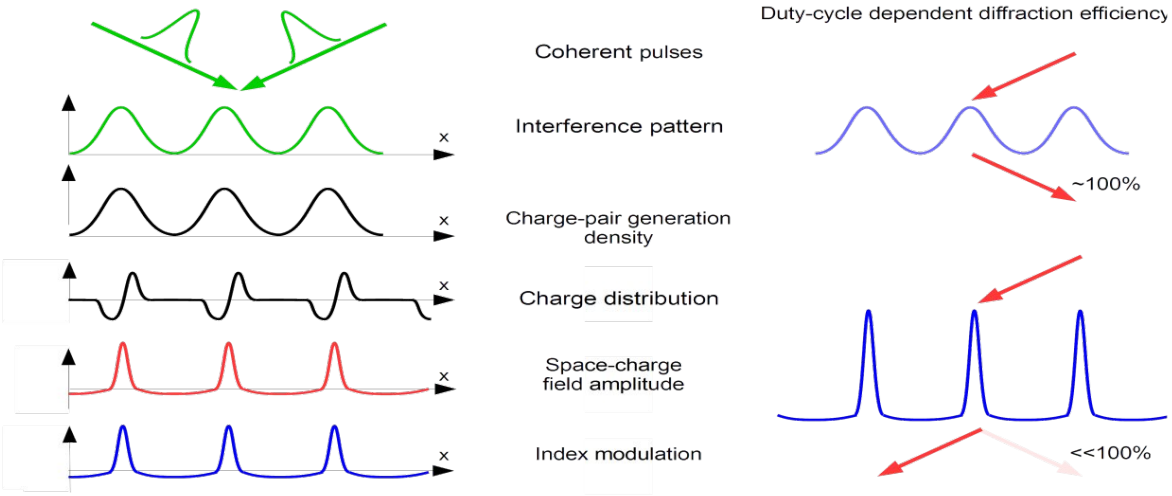

Figure 29: (left) Effect of short pulse illumination of the photoelectric and orientational response of the photorefractive polymer. (right) Effect of the refractive index modulation duty cycle on the diffraction efficiency.

For pulses shorter than about 20μs, decreasing the pulse width causes no significant effect on the diffraction efficiency, indicating that a minimum of a single excitation/transport event has been reached. As shown in Figure 27, the region of interest for 30Hz update rate is in the 1μs to 10μs pulse width range, but the performance of this single APC buffer layer device is relatively weak. Additionally, no gains are made by shifting the pulse length within this range and for no exposure length is the response time fast enough for a video-rate refresh rate.

Removing the buffer layer on subsequent AS-J2 samples increased the maximum diffraction efficiency by shifting the over-modulation inflection to higher voltage and increasing the speed of the grating formation. The responsivity of the photorefractive polymer was high enough that a moderate voltage of 72.5V/μm achieved significant gains in diffraction speed and magnitude. At a constant pulse length of 10μs and a bias of 72.5V/μm, Figure 28a shows the refractive index grating growth and decay dynamics in response to pulses of various energies. The constant time to peak diffraction indicates that the 10μs pulse is well within the single charge

excitation/transport event regime while the increase in peak diffraction efficiency (and rate of rise) with increasing pulse energy appears to slow above 20mJ/cm^2 and nears saturation above 30mJ/cm^2 (Figure 28b). This indicates that there is a negligible benefit to increasing the pulse energy above 30mJ/cm^2 with respect to increasing the speed or magnitude of the diffractive response. With constant pulse energy of 30mJ/cm^2, the diffraction efficiency across the nano- to microsecond range of pulse widths is relatively constant, shown in Figure 30. Compared to the performance of the buffered device, the magnitude of the diffraction efficiency increased by a factor of five from 2.1% to 11% while at the same time decreasing the time of grating formation by a factor of five (from 82ms to 16ms).

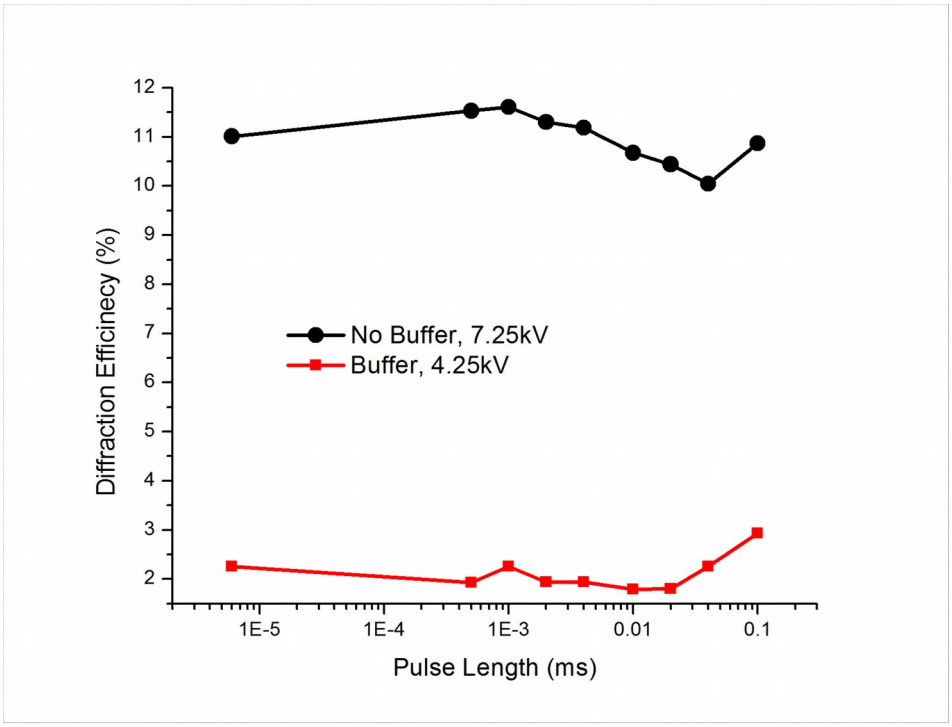

Figure 30: Diffraction efficiency across range of pulse lengths for AS-J2 with and without a buffer layer.

Results of this research are being prepared to be submitted for publication.

Significant Publications:

1. B. Lynn et al., "Real-time imaging of chromophore alignment in photorefractive polymer devices through multiphoton microscopy" Accepted for publication in MRS Communication 2015.

2. P.-A. Blanche, "Photorefractive polymers for 3D display application", Chapter in "Optical Properties of Functional Polymers and Nano Engineering Applications", V. Jain and A. Kokil ed., CRC Press Taylor and Francis, December 2014.

3. S. Jolly et al., "Direct fringe writing architecture for photorefractive polymer-based holographic displays: analysis and implementation", Opt. Eng. 52(5), 055801 (May 07, 2013).

4. B. Lynn et al., "Photorefractive polymer for holography", review article, Journal of Polymer Science Part B: Polymer Physics, 2014 (52), pp 193-231, (November 2013).

5. C. Liebig et al. "Achieving enhanced gain in photorefractive polymers by eliminating electron contributions using large bias fields", Optics Express 21 (25), pp 30392-30400 (2013).

6. B. Lynn et al., "Recent advancements in photorefractive holographic imaging", Journal of Physics: Conference Series 415 (2013) 012050.

7. P. St Hilaire et al., "Are stereograms holograms? A human perception analysis of sampled perspective holography", Journal of Physics: Conference Series 415 (2013) 012035.

8. P.-A. Blanche, "Toward the Ultimate 3D Display", Information Display, February/March vol.28, No.03. 2012.

9. P. P. Banerjee et al., "Time dynamics of self-pumped reflection gratings in a photorefractive polymer", Journal of Applied Physics, vol. 111, 013108, 2012.

10. P.-A Blanche et al., Ch10 and 11 in "Optical and digital Image Processing Fundamentals and Applications", G. Cristobal, P. Schelkens, and H. Thienpond Eds., Wiley-VCH, (2011).

11. C. W. Christenson, C. Greenlee, B. Lynn, J. Thomas, P.-A. Blanche, R. Voorakaranam, P. St. Hilaire, L. J. LaComb, Jr, R. A. Norwood, M. Yamamoto, and N. Peyghambarian, "Interdigitated coplanar electrodes for enhanced sensitivity in a photorefractive polymer", Optics Letters 36, 3377 (2011).

12. N. Peyghambarian et al., "Photorefractive polymers for holographic 3-D display". Selected in Optics and Photonics News, "Optics in 2011", Vol. 22, No. 12, December 2011.

13. J. Thomas et al., "Photoconducting Polymers for Photorefractive 3D Display Applications", Chemistry of Material, Review article, vol. 23, pp 416-429, (2011).

Patents:

- A. Bablumyan, P.-A. Blanche, N. Peyghambarian, "System for Holography", Patent US 8634119, published on January 21th, 2014.
- P.-A. Blanche, A. Bablumyan, N. Peyghambarian, "Auto Stereoscopic 3D Telepresence Using Integral Holography". Patent US 8,334,889, published on December 18, 2012.
- P.-A. Blanche, A. Bablumyan, N. Peyghambarian, "System and method for synchronizing a spatial light modulator with a pulsed laser to record a hologram at the repetition rate of the pulsed laser". Patent US 8,325,402, published on December 4th, 2012.

AFOSR Deliverables Submission Survey

Response ID:4551 Data

1.

1. Report Type

Final Report

Primary Contact E-mail
Contact email if there is a problem with the report.

lschadler@optics.arizona.edu

Primary Contact Phone Number
Contact phone number if there is a problem with the report

520-621-5821

Organization / Institution name

University of Arizona

Grant/Contract Title
The full title of the funded effort.

Development of New Photorefractive Polymer Materials

Grant/Contract Number
AFOSR assigned control number. It must begin with "FA9550" or "F49620" or "FA2386".

FA9550-10-1-0207

Principal Investigator Name
The full name of the principal investigator on the grant or contract.

Nasser Peyghambarian

Program Manager
The AFOSR Program Manager currently assigned to the award

Charles Lee

Reporting Period Start Date

05/01/2010

Reporting Period End Date

04/30/2015

Abstract

The goal of this program was to develop highly efficient photorefractive (PR) polymer material for applications of interest to the Air Force. During the period of this report, we have demonstrated a new interdigitated coplanar geometry for the electrodes of the photorefractive device that enhances its sensitivity and allows diffraction with symmetrically incident beams, a configuration that was not possible with the conventional top and bottom electrodes. Related to this new electrode configuration, we measured the electric field strength inside the material with the help of a multiphoton microscope and were able to identify unsuspected asymmetry due to the photoconduction properties of the polymer matrix. The observed field nonlinearity has led to a revision of the theory governing the diffraction efficiency with coplanar electrode.

Distribution Statement

This is block 12 on the SF298 form.

Distribution A - Approved for Public Release

Explanation for Distribution Statement

If this is not approved for public release, please provide a short explanation. E.g., contains proprietary information.

SF298 Form

Please attach your SF298 form. A blank SF298 can be found here. Please do not password protect or secure the PDF The maximum file size for an SF298 is 50MB.

SF298 FA9550-10-1-0207.pdf

Upload the Report Document. File must be a PDF. Please do not password protect or secure the PDF . The maximum file size for the Report Document is 50MB.

Final Report FA9550-10-1-0207.pdf

Upload a Report Document, if any. The maximum file size for the Report Document is 50MB.

Archival Publications (published) during reporting period:

Changes in research objectives (if any):

Change in AFOSR Program Manager, if any:

Extensions granted or milestones slipped, if any:

AFOSR LRIR Number

LRIR Title

Reporting Period

Laboratory Task Manager

Program Officer

Research Objectives

Technical Summary

Funding Summary by Cost Category (by FY, $K)

	Starting FY	FY+1	FY+2
Salary			
Equipment/Facilities			
Supplies			
Total			

Report Document

Report Document - Text Analysis

Report Document - Text Analysis

Appendix Documents

2. Thank You

E-mail user

May 08, 2015 17:01:17 Success: Email Sent to: lschadler@optics.arizona.edu